Experimental investigation of the influence of nanoparticles on droplet spreading dynamics and heat transfer during early stage cooling

Y T Aksoy, Guillaume Castanet, P Eneren, A C García-Wong, T Czerwiec, O Caballina, M R Vetrano

Experimental investigation of the influence of nanoparticles on droplet spreading dynamics and heat transfer during early stage cooling

Y.T. Aksoy [a,*], G. Castanet [b], P. Eneren [a], A.C. García-Wong [c], T. Czerwiec [c], O. Caballina [b], M.R. Vetrano [a]

[a] KU Leuven, Department of Mechanical Engineering, Division of Applied Mechanics and Energy Conversion (TME), B-3001 Leuven, Belgium
[b] Université de Lorraine, CNRS, LEMTA, F-54000 Nancy, France
[c] Université de Lorraine, CNRS, Institut Jean Lamour, F-54000 Nancy, France

A B S T R A C T

With the increasing interest in improving high-performance cooling systems, research on droplet cooling requires more complex methods for enhancing heat transfer. Hence, we investigate the effect of nanoparticle presence and concentration on droplet spreading dynamics and heat transfer during the early stages of spreading on a heated surface. For this purpose, water and three water-based TiO_2 nanofluid droplets (0.2, 0.5, and 1 wt%) are tested at four release heights impinging on a sapphire substrate below boiling point (80 °C). With an emissive TiAlN coating in the infrared (IR) domain, the surface temperature of the substrate is measured via a high-speed IR thermal camera. Droplet spreading is simultaneously monitored with two high-speed black/white cameras. The thermal and rheological properties are experimentally characterized for accurate results and to investigate only the nanoparticle presence in the fluid. The captured temperature fields are analyzed by solving the inverse heat conduction problem. We observe that all nanofluid droplets spread on a heated surface marginally less than water droplets. To the best of the authors' knowledge, this study is the first to reveal that during the early stages of droplet spreading, the presence of nanoparticles and the resulting change in viscosity primarily influence heat transfer through the modification of the droplet spreading diameter, rather than changes in thermal properties.

1. Introduction

The demand for high-performance electronic devices and chips has triggered the need for more efficient cooling techniques. Spray cooling is a traditional approach used in numerous industrial processes to control heat dissipation at high temperatures. While spray cooling is widely regarded as a state-of-the-art technique, further improvements are under investigation. Among them, replacing traditional coolants with nanofluids, i.e., nanoparticle-laden fluids, still receives considerable attention [1]. Nanofluids, as a new class of fluids for heat transfer, do not only offer improvements in effective thermal conductivity compared to their base fluid but also are expected to overcome usual problems with bigger particles, such as sedimentation, clogging, increased pressure drop, and erosion of the spraying system. However, the heat transfer process gets complicated compared to the traditional fluids, ending up with contradictory outcomes in several studies [2]. The exact mechanisms through which heat transfer is affected by nanoparticles are still in debate. In this regard, the postulated mechanisms, such as thermal conductivity enhancement, nanoparticle deposition, or modified wetting, must be distinguished to explain the physical phenomena. For example, the droplet spreading/splashing dynamics on a solid surface can be modified, and in some cases, it may even allow the control of the spreading diameter [3]. Indeed, the addition of nanoparticles to the base fluid can also be utilized to tune the wettability on a solid surface and help regulate droplet spreading as a function of nanoparticle concentration [4,5]. Since surface wettability is one of the key factors in the heat transfer process, the thermal and hydrodynamic behavior of nanofluid droplets must be simultaneously assessed during droplet spreading.

The impact of a single droplet, excluding nanoparticles, on a heated solid surface is already well documented [6]. Nevertheless, heat transfer during a single droplet impact and spreading is already complex due to the interplay between the impact momentum and the spreading dynamics. To take into account the physical phenomena related

to droplet dynamics, these non-dimensional numbers are commonly used: Weber number $We = \rho u_0^2 D_0/\sigma$ for inertia/surface tension forces, Reynolds number $Re = \rho u_0 D_0/\eta$ for inertia/viscous forces, and Ohnesorge number $Oh = \sqrt{We}/Re$ for viscous forces/inertia and surface tension forces with the material properties density ρ, viscosity η, and surface tension σ with impact parameters impact velocity u_0 and initial diameter before impact D_0 [7,8]. The temperature of the solid surface also plays a critical role by influencing the impact dynamics and heat transfer performance. In fact, several regimes can be observed with increasing surface temperature: film evaporation, nucleate boiling, transition boiling, and film boiling [9]. More specifically, comprehensive heat transfer models are required to deal with conduction across the liquid film, internal motion, and convection within the droplet. In the film evaporation regime, a better understanding of the impact behavior, from the onset of impingement and during subsequent oscillations leading to the shape equilibrium moment, would greatly improve heat transfer models. Despite some numerical attempts considering the droplet spreading mechanism with thermal evaporation [10], it is so far challenging to predict the real effects of the nanoparticles.

From an experimental point of view, several imaging techniques can be used. For example, Gholijani et al. [11] simultaneously employ an infrared thermal camera (IRC) and a high-speed black/white camera (HSC) to evaluate the effect of wall superheat, impact velocity, and spreading diameter on heat transfer and droplet dynamics. If those parameters are increased, heat flow also increases owing to the higher temperature difference between the heated surface and droplet, and larger spreading. Nevertheless, the wall superheat deteriorates droplet spreading due to the increased evaporation rate in the vicinity of the three-phase contact line. Guggilla et al. [12] study a train of two droplets concentrically impinging on a heated surface. Since higher heat transfer rates occur in the region of the three-phase contact line, an increased spreading film thickness (a reduced surface-to-volume ratio) in drop-on-drop cases results in a decline in heat transfer. The dependence of heat flow on the spreading diameter rather than the contact area is explained as a result of the effect of Marangoni forces and the cooling by the evaporation being highest near the contact line [11–13]. Gholijani et al. [14] further investigate the influence of wall superheat and the generation frequency of successive droplets. They report that the maximum contact line and maximum heat flow due to the second droplet do not significantly depend on the droplet generation frequency as the shape and temperature do not change rapidly in the former droplet, which can be considered sessile.

Okawa et al. [15] observe that water-based TiO_2 nanofluid droplets significantly improve heat transfer in the nucleate boiling regime when the wall superheat is not too high (below 250 °C). Moreover, the critical heat flux compared to their base liquid is approximately 50% higher. They also document that a thin deposited nanoparticle layer on the substrate surface accumulated from the previous droplets improves the solid–liquid contact. On the other hand, heat transfer can be augmented by the presence of nanoparticles due to the modified surface wettability. For instance, Jackson et al. [16] claim that double-walled carbon nanotubes (DWCN) enhance the transient cooling more on hydrophilic surfaces, where DWCN concentration does not affect the heat transfer rate. In another study, Liu et al. [10] speculate that the buoyancy forces alter the local velocity direction near the contact area as a result of a layered temperature gradient. Pournaderi et al. [17] numerically investigate the water-based Al_2O_3 nanofluid droplet impact on a heated surface. Up to a certain nanoparticle concentration, the heat transfer rate increases, which is almost independent of the impact velocity. Siddiqui et al. [18] discuss the effect of the mixing ratio of the silver nanoparticles and graphene nano-platelets during the evaporation of a droplet. The optimum mixing ratio for the fastest evaporation is found to differ with the surface temperature. Nanoparticle concentration influences the hydrodynamic characteristics of impinging droplets [3], such as higher spreading diameter owing to possibly more kinetic energy [19]. Similarly, the presence of nanoparticles promotes splashing at low Reynolds numbers with higher lamella spreading speeds due to earlier wetting at isothermal conditions [20]. Pontes et al. [21] elaborate the conditions for the heat transfer enhancement with 0.5% Ag-water and Au-water nanofluid droplets, stabilized via CTAB surfactant. Their results suggest that even though the nanofluid droplets demonstrate larger spreading diameters compared to water, the heat transfer enhancement can only be observed during the earlier stages after the impact (<20 ms) for low-impact velocities (0.8 m/s, Re≈2400). They explain this situation by the local increase of the nanoparticle concentration at the triple contact line due to nanoparticle migration, deposition, and evaporation. Similarly, Jiang et al. [22] focus on the gas–liquid mass transfer of an evaporating sessile nanofluid droplet. Optimal nanoparticle concentration would improve the mass transfer efficiency (the ratio of nanofluid droplet volume change to that of water) as nanoparticles have the potential to generate additional mass diffusion, i.e., micro-convective mass transfer. This effect is more prominent with the smaller particles owing to the promoted Brownian motion.

This paper aims to experimentally evaluate the influence of the nanoparticles, present in the base fluid, on both the droplet spreading dynamics and the cooling performance. In particular, we examine water-based TiO_2 nanofluid droplets impacting a heated TiAlN-coated flat sapphire substrate whose temperature is fixed below the boiling point of the base fluid to remain in the film evaporation regime. The focus is first placed on the analysis of the droplet spreading. The maximum spreading diameter is measured for various impact velocities and nanoparticle concentrations. Then, a comprehensive heat transfer analysis of the droplet cooling is carried out. Solving the inverse heat conduction problem accurately quantizes heat removed from the substrate. The heat transfer during droplet spreading is compared for different impact cases to show the influence of the nanoparticles.

2. Materials and experimental methods

Characterizing the heat transfer process during the impact of an individual droplet is not straightforward. Measuring the evaporation lifetime is insufficient to evaluate the heat transfer performance in most cases. More in detail, thermal conduction plays a dominant role at the beginning of the droplet impact due to the high-temperature difference between the droplet and the solid surface. Then, evaporation progressively contributes while the liquid temperature approaches saturation. Also, at the beginning of the droplet impact, the presence of nanoparticles can modify the dynamics of the contact line. To gain some insight into the cooling process, it is essential to quantify the heat transfer in a time-resolved manner. This can be done with temperature measurements at the heated solid surface or by measuring the liquid temperature during the spreading [23,24]. In this study, the temperature evolution of the heated surface is observed using a high-speed IRC. Basically, the approach consists of a substrate transparent in the infrared (IR) spectra, whose surface is coated with a thin layer of an IR emissive material [14,25]. This thin emissive coating allows monitoring of the temporal and spatial evolution of the contact temperature between the substrate and the liquid at a high temporal resolution. Finally, the local heat flux is derived from these measurements by solving the transient heat conduction problem inside the solid substrate, either numerically [11] or based on an analytical model [26].

2.1. Experimental setup and conditions

Fig. 1 illustrates the experimental setup. The syringe pump infuses the working fluid through a needle to form a millimeter-size droplet. The droplets are released onto a heated sapphire substrate at different heights, i.e., 10, 15, 20, and 25 cm, to vary the impact velocity u_0 (1.45–2.30 m/s). The temperature of the substrate can be adjusted owing to four cartridge heaters inserted into a steel holder where

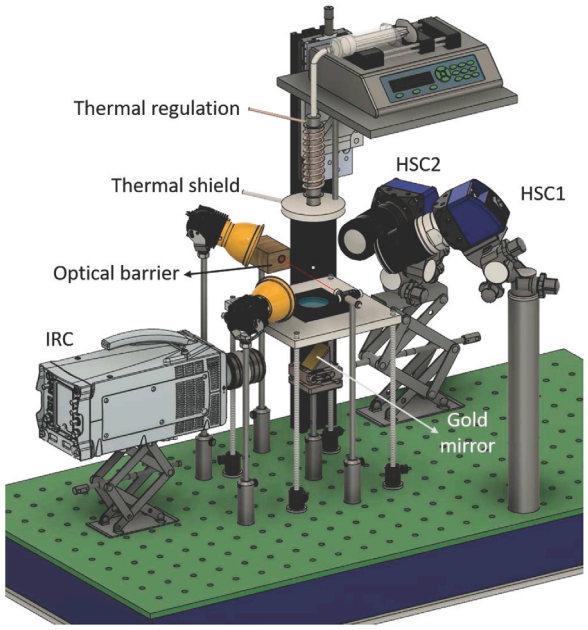

Fig. 1. Experimental setup characterizing droplet spreading dynamics and heat transfer performances of water and water-based TiO_2 nanofluids impacting onto the heated sapphire substrate.

the cylindrical sapphire substrate (diameter of 2.54 cm, thickness of 5 mm) is placed. The focus is given to the heat transfer and droplet dynamics in the film evaporation regime, and the substrate temperature is set at 80 °C for all experiments. Thus, the thermal properties of the sapphire at 80 °C are used for heat capacity ($C_{p_{\text{sapphire}}}$ = 899.68 J/kg K) and the thermal conductivity (k_{sapphire} = 29.51 W/m K) in accordance with [27,28]. The temperature of the liquid upstream of the needle tip is thermally regulated at 24 °C by using a heat exchanger. In addition, the droplet is formed within a few-mm small cavity in a thermal shield, which protects the droplet from the hot air plumes arising from the heated substrate. Hence, a constant and perfectly known initial droplet temperature is imposed regardless of its release height h. To characterize the heat transfer between the droplet and the sapphire substrate, the same technique in [26] is implemented based on high-speed IR thermography. Due to the fact that both the sapphire transparency and the TiAlN emissivity are quite high in the IR region (< 5 μm), the sapphire is coated with a thin layer of TiAlN so that the evolution of the sapphire temperature at the upper side can be monitored during droplet spreading by means of a gold mirror tilted at 45°.

The TiAlN film is grown on the sapphire substrate by reactive magnetron sputtering of the Ti and Al targets (diameter of 5.08 cm each) in a mixture of argon and nitrogen with flow rates of 30 and 5 standard cubic centimeters per minute, respectively. The cathodes in the sputtering chamber in a confocal configuration, together with the substrate holder in the rotating mode (15 revolutions per minute), guarantee the good homogeneity of the film. The base pressure is fixed at 0.22 Pa, and the substrate holder is not heated on purpose during the deposition. The Ti target is powered using a DC power supply (Maxime 1000) with a constant discharge current of 0.57 A, while the Al target is powered using a pulsed-DC power supply (Advanced Energy Pinnacle+) with a constant discharge current of 0.5 A. The frequencies of DC pulses and their off-time values are kept at 50 kHz and 4 μs, respectively. The distance between the sapphire substrate and both targets is 9 cm. The deposition rate is 17.4 nm/min, and the time of deposition is adjusted to obtain a film thickness of 2 μm. The small thickness of the TiAlN coating makes it possible to capture surface temperature variations within a fraction of μs. The same coated sapphire substrate is used during the measurement campaign to avoid any change in the surface wetting properties and roughness [29]. The substrate surface is carefully wiped up without harming the TiAlN coating after each impact to eliminate dust and stain. Furthermore, before each measurement, some droplets are released to prevent contamination at the needle tip while the droplet is pending.

Table 1
Image acquisition parameters.

Camera	Frame rate [fps]	Frame size [px]	Shutter time [μs]	Pixel resolution [μm/px]
HSC1 (oblique)	12 000	512 × 432	29	16.82
HSC2 (side)	12 000	512 × 432	29	13.60
IRC	2000	320 × 248	90	66.95

Telops FAST M1k IRC is employed for the temperature measurements of the sapphire substrate at 2000 fps. No spectral filter is applied for the IR signal detection, and the exposure time is fixed at 90 μs to receive sufficient signal variation during the droplet spreading. A gold mirror with high reflectivity in the IR region is placed under the sapphire substrate to direct the view to the thermal camera. Calibration is performed under the same conditions as in the experiments to convert the measured digital levels into temperature. The IRC calibration consists of varied sapphire temperatures while measuring the digital levels of the image. Moreover, the reduction in the signal intensity due to the reflectance at the lower surface of the sapphire and the environmental contributions to the signal are included in this calibration. In parallel, two HSCs (HSC1 and HSC2) (Photron FastCAM-APX RS) in the visible range are employed to record the droplet impact. The shadowgraphy imaging including HSCs helps observe the droplet's dynamic behavior: HSC1 is positioned at an oblique angle with respect to the sapphire surface. Its inclination provides an advantage to clearly observe the structures that develop during the droplet spreading, such as capillary waves and rim projection. HSC2 is horizontally placed to obtain the side view for the initial droplet diameter and the impact velocity. Both cameras acquire shadowgraphy images at 12 000 frames per second (fps) in a 10-bit grayscale with a 1/35 000 s shutter time. The image acquisition parameters for the three cameras are summarized in Table 1. To simultaneously trigger the image acquisition, the droplet fall is realized with an optical barrier. While the droplet crosses the laser beam of the optical barrier, the laser deviation is detected by a photodiode that receives the transmitted light in the absence of a droplet.

h is arranged to adjust the impact velocity to set We and Re numbers covering the ranges of 60–160 and 2750–4750, respectively. The difference in the droplet positions in subsequent frames is divided by the time between the frames to determine the impact velocity. Good droplet circularity of at least 0.93 is always verified during the post-processing. More details about the methodology to evaluate the droplet diameter and the impact velocity from the shadowgraphy images are described in [20].

2.2. Nanofluid preparation and characterization

The nanofluids are prepared at three mass fractions (C_w= 0.2, 0.5, and 1 wt.%) by diluting a stable and well-dispersed TiO_2-water nanofluid suspension (rutile, 40 wt.%, 30–50 nm size range, Io-litec Ionic Liquids Technologies GmbH). During the dilution process, in which only milli-Q water is added (no dispersant/surfactant), a vortex mixer and a sonic bath are employed to ensure good mixing. To verify the particle size distribution and the good dispersity, the diluted nanofluids are tested via the Light Extinction Spectroscopy technique with the procedure explained in [30]. Fig. S1 in the supplementary

Table 2
Measured properties of the samples.

	C_w [%]	$\rho \left[\frac{kg}{m^3}\right]$	$\sigma \left[\frac{mN}{m}\right]$	η [mPa s]	CA [°]
Water	0	996.13	71.00	1.00	89
TiO_2-water	0.2	996.80	68.81	1.02	87
TiO_2-water	0.5	997.79	68.44	1.04	86
TiO_2-water	1	999.46	66.16	1.09	85

information illustrates the size distribution of the nanofluid at 0.2 wt.%. In addition, all samples are experimentally characterized in terms of the density ρ, surface tension σ, and viscosity η as detailed in the supplementary information. The results of these measurements are reported in Table 2 and in agreement with the literature [31–33]. It is documented in the literature that nanoparticles either decrease or increase the surface tension depending on their wettability [34]. If particles form clusters, having larger effective diameters than their actual size, they might sediment and deposit on the substrate. The resultant surface conditions can lead to an increase in the contact angle (CA) [35]. In our case, we see a decrease both in the surface tension and contact angle values with increased nanoparticle concentration, which is consistent with each other and confirms the absence of clustering.

The thermal conductivity of metallic oxide nanofluids depends on temperature, nanoparticle concentration, shape, and size [36]. Thermal conductivity of both nanofluids and water are measured according to the procedure elucidated in [37,38], and the details of the procedure are given in the supplementary information. As seen in Fig. S2 in the supplementary information, the thermal conductivity values of the nanofluids barely differ from that of water due to their low nanoparticle concentration. Limited variations are also observed by Lv et al. [39] for 1 wt.% Al_2O_3 nanofluids within the temperature range of our measurements and Pryazhnikov et al. [40] for various concentrations (up to 6 vol.%) of TiO_2 nanofluids at room temperature. Existing models [2,41] are consistent with a small increase in the effective thermal conductivity, yet so small that it cannot be quantified due to the limitations and uncertainties associated with the measuring device employed.

3. Results and discussions

In this work, the spreading dynamics and heat transfer performance are investigated for water and water-based TiO_2 nanofluid droplets at 0.2, 0.5, and 1 wt.%, which are released from four different heights 10, 15, 20, and 25 cm. To ensure the repeatability of the measurements, each impact condition is repeated at least three times (see repeatability measurements in Fig. S3 in the supplementary information). Fig. 2 exemplifies the simultaneous temporal evolution of a water droplet spreading, the measured temperature fields at the TiAlN-coated surface of the sapphire substrate, and the calculated heat flux densities from these temperature fields (We = 95.5, Re = 3759). More in detail, the last image recorded prior to the droplet impact is assigned to t = 0 ms. Since there is not yet a contact, the uniform substrate surface temperature can be verified. In fact, this first temperature image is used as a reference that is subtracted from the other frames to calculate the surface temperature variation θ in the inverse heat conduction model, whose details are given in the appendix.

At the beginning of the spreading, the rim formed on the edge of the liquid lamella is projected radially. Capillary waves give rise to ridges and troughs on the droplet surface that are visible as light and dark rings in the shadowgraphy images. This pattern is also apparent in the images of IR thermography, which illustrates the close relationship between the droplet dynamics (internal liquid motion, droplet shape, etc.) and the removed heat from the substrate. The high sensitivity of the IR camera with low noise equivalent temperature difference (NETD = 25 mK) allows for capturing these small variations in the surface temperature of the sapphire substrate, which can be as small as a few tenths of °C. The rim extends on the droplet edge during the spreading, while the liquid lamella gets thinner at the center. Then, the droplet edge progressively becomes the region where most of the cooling occurs. It remains so during the receding phase until the droplet elongates vertically after 9.5 ms. This ascending flow is associated with the formation of a cold spot at the center of the droplet. As time passes, thermal relaxation and heat diffusion result in a blurry temperature distribution outside the contact area of the droplet. The droplet spreads radially again after the maximum vertical elongation around t = 17.5 ms. This second spreading is much smaller than the first one due to the loss of kinetic energy by viscous dissipation. Finally, when the adhesion forces at the triple contact line can no longer be overcome by the liquid flow, the triple contact line stagnates, and the internal liquid motion rapidly fades away. After t = 30 ms, the droplet can be considered a sessile droplet, which entirely evaporates in about 1 s. The evaluation of the heat transfer during the pure evaporation phase is beyond the scope of this study.

An inverse heat conduction problem (IHCP) is solved to quantify the heat removed by the droplets from the heated sapphire substrate. The implemented approach is similar to that developed by Chaze et al. [26], whose details are given in the supplementary information. The problem geometry and the axis system definition are given in Fig.S4 in the supplementary information. The heat flux q shown in Fig. 2 is computed under the axisymmetry assumption via this method using the temperature difference profiles, from the center (r = 0) in the radial direction (r), as depicted in Fig. S5 in the supplementary information. After an initial rise, it can be noticed that q exhibits a decline as time progresses. For the thermal contact between two semi-infinite media initially at different temperatures, it is known that the heat flux scales with time $t^{-1/2}$ [42]. In our case, a similar evolution is observed despite the complex dynamics of the droplet and its finite volume since the thermal diffusion length is below 65 μm during the analysis time (see supplementary information). From these results, the temporal evolution of the global heat flow Q can be determined by spatial integration of $q(r,t)$ from the impact center to cover the whole cooled region (r = R):

$$Q(t) = 2\pi \int_{r=0}^{R} q(r,t) \cdot r \; dr. \tag{1}$$

Fig. 3 demonstrates both the temporal evolutions of Q and the spreading diameter D normalized with respect to D_0, i.e., spreading ratio β, for the same experiment, as reported in Fig. 2.

For a short instant just after the impact (t < 3 ms), both Q and β rapidly rise until the maximum spreading is achieved as the contact area between the initially cold liquid and the heated surface enlarges. However, as the droplet temperature gradually increases at the contact area, the increase in the spreading diameter is no longer sufficient to compensate for the decay of q. The consequent decrease in Q occurs at a faster rate than the spreading ratio due to both decreasing contact area and increasing liquid temperature there. The heat flux reaches a plateau of low values (≈12–14 ms) even before the end of the receding phase (≈19 ms). Following the vertical elongation, a very small increase in the heat flow occurs during the second spreading of the droplet (t> 20 ms). After stabilization of the triple contact line (≈27 ms), Q also stabilizes at a low but non-zero value. Afterward, only evaporation takes place, involving the latent heat, for the rest of the droplet's life. In addition, Q augments with h as well as the maximum spreading diameter, since the contact area mainly controls heat transfer (see Fig. S6 in the supplementary information).

To further compare the total heat removed from the surface among different concentrations of TiO_2 nanoparticles, Q is integrated over time $E = \int Q(t)\,dt$. In this way, the uncertainties due to the impact moment are also eliminated. The subtraction of a reference image recorded prior to impact also allows the suppression of parasitic radiations coming from the ambient and possibly from the steel holder. Another

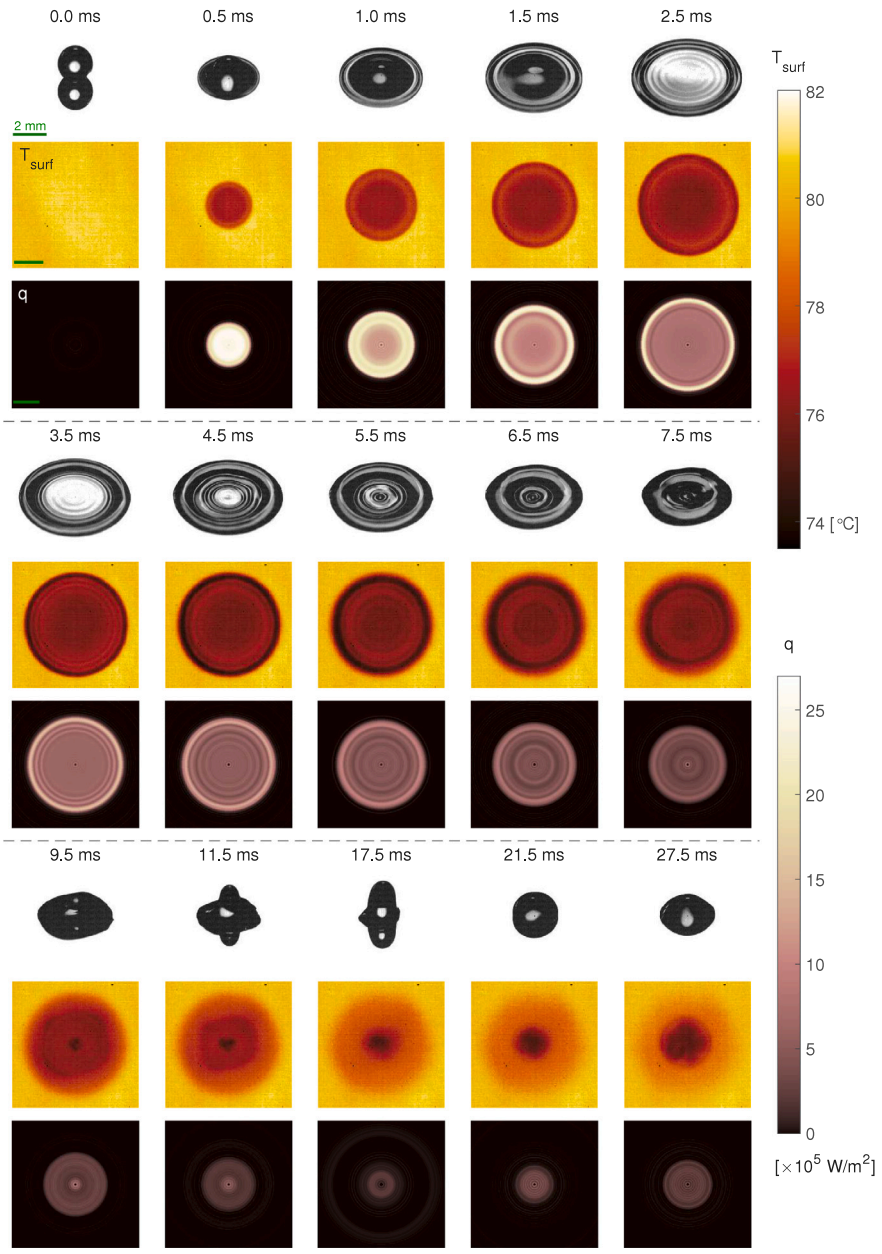

Fig. 2. Time evolution of a spreading water droplet (We = 95.5, Re = 3759) on the TiAlN-coated heated sapphire substrate. First row: shadowgraphy images. Second row: substrate temperature field T_{surf}. Third row: reconstructed heat flux q by the solution of the inverse heat conduction problem (IHCP). Green lines in each image set indicate 2 mm.

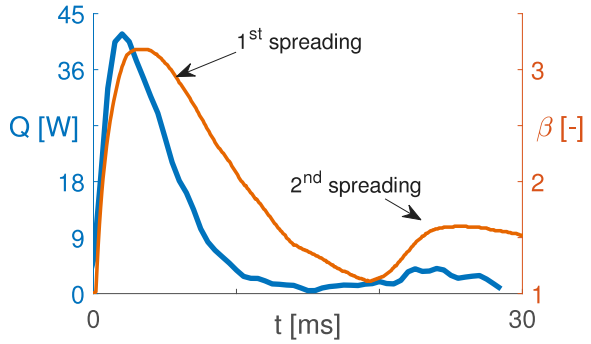

Fig. 3. Time evolution of the global heat flow Q and the normalized diameter β for the same case of water droplet as in Fig. 2.

uncertainty source would originate from the thermal properties of the sapphire substrate since they are retrieved from the literature rather than experimental characterization. However, this introduced error on the absolute values is also eliminated in the comparative results by using the same sapphire substrate throughout the entire study, allowing conclusive comparisons among the different concentrations of nanoparticles. Taking into account the uncertainties in the surface (smaller than 0.2 °C) and droplets' initial (smaller than 1 °C) temperature measurements and repeating the measurements several times under the same conditions, the final uncertainty in energy is estimated to be around 5 mJ. This value agrees well with the value of 7.2 mJ in the previous study of Castanet et al. on droplet impact in the Leidenfrost regime [43]. Additionally, this uncertainty is further minimized by the assumption of axisymmetry for the IHCP solution, requiring pixel averaging, reduction of parasitic radiations from the sapphire substrate owing to the high-emissivity coating, and spatial filtering of the off-field radiations.

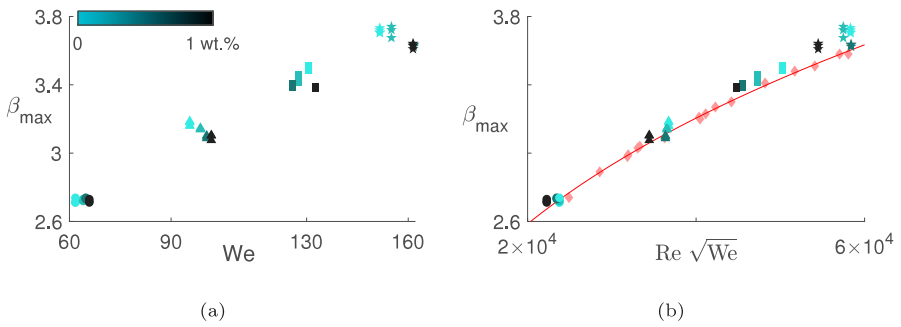

Fig. 4. Maximum droplet spreading ratio β_{max} as a function of (a) We number and (b) Re$\sqrt{We}$ on the sapphire substrate. The pink diamonds illustrate the impact of water droplets on the same surface at isothermal conditions. The model [44,45] is also plotted by the solid red line. The color gradient expresses the TiO_2 nanoparticle concentrations in droplets (0, 0.2, 0.5, and 1 wt.%) and the nondimensional numbers are varied due to different h values: 10 cm (circles), 15 cm (triangles), 20 cm (squares), 25 cm (stars).

3.1. Effect of TiO_2 nanoparticles on droplet spreading dynamics

The variation of the Weber number with respect to the maximum droplet spreading ratio β_{max} (ratio of the maximum spreading diameter D_m to D_0) is presented in Fig. 4(a). As expected, β_{max} increases for all samples with increasing We number, whose variation is mainly driven by the h. Differences appear to be distinctive between the nanofluid and the water droplets as the We number increases and β_{max} decreases with increasing nanoparticle concentration. Therefore, to include these effects of modifications in viscosity due to nanoparticle addition, β_{max} is plotted as a function of Re$\sqrt{We}$ in Fig. 4(b), following the power law (solid red line) [44–46]. Clearly, there is no longer the same scattering of the data using the parameter Re$\sqrt{We}$. In the same figure, also water droplets spreading on the same surface, yet in isothermal conditions (pink diamonds), are plotted. At greater h values, i.e., higher Re$\sqrt{We}$, the droplet spreading becomes slightly larger for the heated cases compared to the isothermal ones. Although at a fixed We number (Fig. 4(a)), the maximum spreading gets slightly smaller while increasing the nanoparticle concentration, their effect is negligible as a function of Re$\sqrt{We}$.

3.2. Effect of TiO_2 nanoparticles on heat transfer

Fig. 5 presents the temporal evolution of the cumulative energy E extracted from the surface by the droplets having TiO_2 nanoparticle concentrations of 0, 0.2, 0.5, and 1 wt.% and the h values of 10, 15, and 25 cm. E is evaluated via the integration of $Q(t)$ over a time period of 15 ms, covering the spreading phase and most of the receding phase. Since E is the time integral of Q, it drastically increases over time until Q reaches the plateau. Then, E exhibits a slightly increasing trend for all cases, which corresponds to the evaporation-dominant phase. However, regarding the effect of nanoparticle concentration, E decreases with the increasing nanoparticle concentration invariant of the h. Although the differences are not very pronounced, the accuracy of our measurements (on the order of 5 mJ) is sufficient to evidence this effect of the nanoparticle concentration.

Fig. 6 shows the removed heat E as a function of We and Re numbers, in which the effect of the nanoparticle concentration is more clearly observed compared to Fig. 5. For a given We number, the higher the TiO_2 nanoparticle concentration in the droplet, the lower the cooling of the TiAlN-coated sapphire substrate.

Several explanations can be proposed for this reduction in heat transfer with the TiO_2 nanoparticle concentration. The first one would be a deterioration in the thermal properties of the nanofluid. To account for this reduced cooling, it would be necessary that the thermal properties of nanofluids, such as thermal conductivity (k) and thermal diffusivity ($k/\rho C_p$), decrease with the increasing TiO_2 nanoparticle concentration. However, a precise evaluation of these properties indicates that these are very weakly affected, e.g., typically less than 1% when water and nanofluid at 1 wt.% are compared. Also, not more than 1 % change in thermal conductivity is expected at low TiO_2 nanoparticle loading [47,48]. Consequently, this marginal change in the thermal properties of the liquids (Fig. S2 in the supplementary information) does not seem to be the main reason for the differences observed in Fig. 6. In Fig. 6(b), it is apparent that E correlates well with the Re number, independent of the nanoparticle concentration. This implies that the main influence of the nanoparticles is induced through viscous dissipation. In other words, by altering the surface tension and the dynamic viscosity of the liquid, the presence of the nanoparticles adversely affects the spreading of the droplet, and thus the cooling area (see Fig. 4(b)). To correlate the droplet spreading and the heat transfer, E is plotted in Fig. 7 as a function of both the β_{max} and the time-averaged spreading ratio $\bar{\beta}$, as defined in (2).

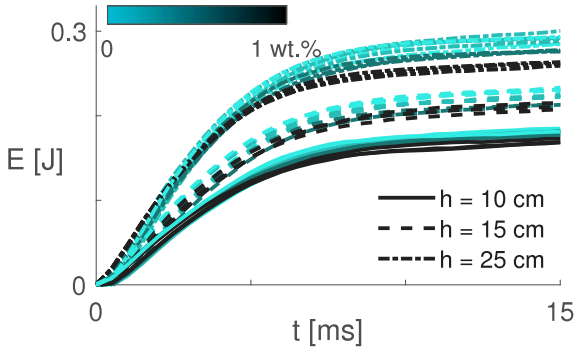

Fig. 5. Temporal evolution of the removed heat E from the sapphire substrate. The color gradient expresses the TiO_2 nanoparticle concentrations in droplets (0, 0.2, 0.5, and 1 wt.%). For the sake of clarity, the results from the h of 20 cm are not displayed nor are the error bars corresponding to 5 mJ.

$$\bar{\beta} = \frac{1}{D_0}\sqrt{\frac{1}{t_f}\int_0^{t_f} D(t)^2 dt}, \tag{2}$$

where the final time t_f is set to 15 ms following the previous calculation of E. The layout of the data points in Figs. 7(a) and 7(b) reveals no dramatic effect of the presence of TiO_2 nanoparticles on the evolution of E as a function of β_{max} and $\bar{\beta}$. Nevertheless, the data in Fig. 7(b) is more scattered than in Fig. 7(a). This suggests that most of the heat (other than evaporation) is removed until the droplet reaches its maximum spreading, which is in accordance with Fig. 3.

Finally, we also account for the mass difference among the droplets by normalizing E by the droplet mass (m). Since adding nanoparticles increases the density and decreases the surface tension, the pendant droplet detaches from the tip of the needle with a slightly smaller volume. As a consequence, these two competing phenomena yield marginally lighter droplets whose masses, however, can accurately be calculated from the images of the droplets before the impact. This is eased by the fact that the droplets are almost perfectly spherical. On the

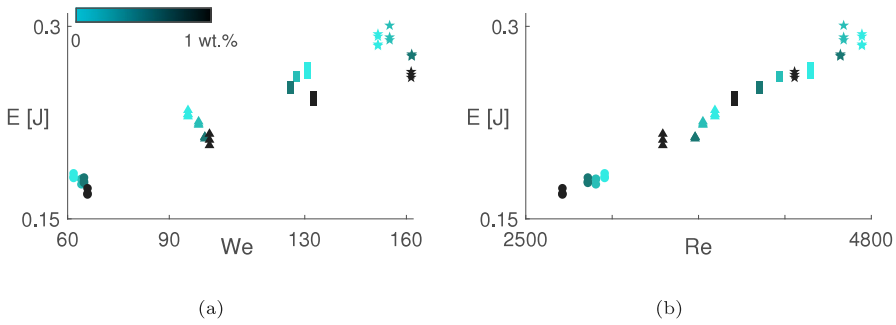

Fig. 6. The removed heat E from the substrate within the first 15 ms of the droplet spreading as a function of (a) We and (b) Re numbers. The color gradient expresses the TiO_2 nanoparticle concentrations in droplets (0, 0.2, 0.5, and 1 wt.%) and the nondimensional numbers are varied due to different h values: 10 cm (circles), 15 cm (triangles), 20 cm (squares), 25 cm (stars).

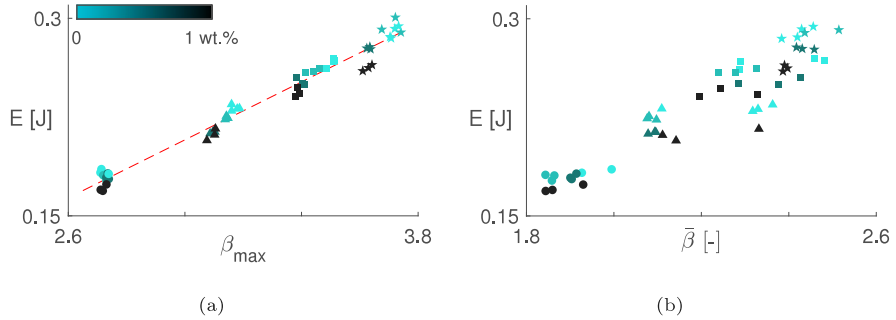

Fig. 7. The influence of (a) the maximum spreading ratio β_{max} and (b) the time-averaged spreading ratio $\bar{\beta}$ on the removed heat E from the sapphire substrate after 15 ms of the droplet impact. The color gradient expresses the TiO_2 nanoparticle concentrations in droplets (0, 0.2, 0.5, and 1 wt.%). The red dashed line linearly fits the experimental data.

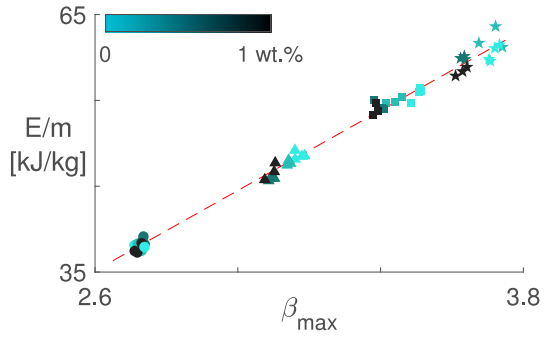

Fig. 8. The removed heat E from the substrate after 15 ms of the droplet impact is normalized by the initial droplet mass. The color gradient expresses the TiO_2 nanoparticle concentrations in droplets (0, 0.2, 0.5, and 1 wt.%) and the nondimensional numbers are varied due to different h values: 10 cm (circles), 15 cm (triangles), 20 cm (squares), 25 cm (stars).

contrary, the heat capacity of the nanofluid droplets does not vary at these small concentrations as in the case of thermal conductivity [2]. To better reflect this outcome, the mass-normalized heat removal (E/m) is plotted against β_{max} in Fig. 8, which displays their linear relation. Once again, this suggests that the heat transfer is mainly driven by the maximum spreading diameter reached in the first few ms after the impact. The presence of nanoparticles lowers the cooling performance at a fixed value of h since it reduces the maximum droplet spreading, and thus the surface for the heat exchange. This effect prevails over the change in the thermal properties induced by the presence of nanoparticles.

4. Conclusions and perspectives

In this study, we mainly focus on the influence of the rutile TiO_2-water nanofluids on droplet spreading and heat transfer on a heated flat TiAlN-coated sapphire substrate. The nanofluids (0.2, 0.5, and 1 wt.%) are prepared and experimentally characterized in terms of their rheological properties, stability, and thermal conductivity. To correlate the droplet dynamics to the heat transfer, two high-speed black/white cameras and one high-speed infrared thermal camera are used. The impact velocity and the non-dimensional numbers are varied due to various release heights of 10, 15, 20, and 25 cm. Each impact case is repeated at least three times.

An inverse heat conduction problem is solved to evaluate the heat flux and total energy removed from the sapphire substrate by the nanofluid droplets. As expected, the maximum spreading ratio increases with the increasing We number, thus improving the cooling performance. On the other hand, at any We number, increasing TiO_2 nanoparticle concentration leads to a smaller droplet spreading, which is mainly driven by the viscous dissipation caused by the addition of nanoparticles. In the end, a linear relationship between the energy removed from the substrate per droplet mass and the maximum spreading diameter is obtained regardless of the nanoparticle concentration. Therefore, it can be deduced that heat transfer particularly depends on the spreading diameter rather than the change in the thermal properties due to nanoparticle addition which agrees with the literature such that higher heat transfer rates occur in the region of the three-phase contact line [12]. If one excludes the nanoparticle deposition effects [49], surface roughness modification [50], surfactant contributions [21], and material removal problems [51] within the framework of this study, only the net effect of the presence of the nanoparticles remains. To conclude, nanofluid droplets with further spreading properties are foreseen to enhance heat transfer performance although this is not achieved with the current water-based TiO_2 nanofluids.

We also measure the nanoparticle size distribution via Light Extinction Spectroscopy, in which the median diameter lies a little bit outside of the company specifications. Since nanoparticle clustering is inevitable in many applications due to the van der Waals forces and other colloidal interactions among the nanoparticles, this phenomenon should be regarded before industrial use in heat transfer applications.

As solely numerically studied [17], the assessment of particle gradient within the spreading droplet, i.e., higher nanoparticle concentration close to the substrate, would be an interesting future work since this might be a reason for the heat transfer enhancement by sub-cooled nanofluid droplets. Moreover, the nanofluid use in combination with the optimized surface structures might still enrich the heat transfer process with future research in the sustainability of the cooling systems [52].

CRediT authorship contribution statement

Y.T. Aksoy: Conceptualization, Methodology, Software, Validation, Formal analysis, Investigation, Writing – original draft, Writing – review & editing, Visualization, Project administration. **G. Castanet:** Methodology, Software, Formal analysis, Investigation, Resources, Writing – original draft, Writing – review & editing, Supervision, Funding acquisition. **P. Eneren:** Conceptualization, Methodology, Investigation, Resources, Writing – original draft, Writing – review & editing, Visualization. **A.C. García-Wong:** Resources, Writing – original draft, Writing – review & editing. **T. Czerwiec:** Resources, Writing – original draft, Writing – review & editing. **O. Caballina:** Methodology, Software, Formal analysis, Resources, Writing – original draft, Writing – review & editing, Supervision. **M.R. Vetrano:** Resources, Writing – original draft, Writing – review & editing, Supervision, Project administration, Funding acquisition.

Declaration of competing interest

The authors declare that they have no known competing financial interests or personal relationships that could have appeared to influence the work reported in this paper.

Data availability

Data will be made available on request.

Acknowledgments

This work is supported by Interne Fondsen KU Leuven/Internal Funds KU Leuven (C3/21/029). The authors are grateful to the French national research agency ANR for its support of the research program DROPSURF (ANR-20-CE05-0030). The authors also acknowledge Dr. Nicolò Sgreva and Dr. Mykola Isaiev for the thermal conductivity measurements of water and nanofluid samples. The authors are also grateful to the Centre de Compétences of the Institut Jean Lamour for the sputtering chamber provision. The authors also appreciate the in-kind support of the Department of Chemical Engineering, KU Leuven for the nanofluid characterization devices.

Appendix A. Supplementary data

Supplementary material related to this article can be found online at https://doi.org/10.1016/j.expthermflusci.2023.111023.

References

[1] S.M.S. Murshed, Heat transfer and fluids properties of nanofluids, Nanomaterials 13 (7) (2023) http://dx.doi.org/10.3390/nano13071182.

[2] Y.T. Aksoy, Y. Zhu, P. Eneren, E. Koos, M.R. Vetrano, The impact of nanofluids on droplet/spray cooling of a heated surface: A critical review, Energies 14 (1) (2021) http://dx.doi.org/10.3390/en14010080.

[3] Y.T. Aksoy, L. Liu, M. Abboud, M.R. Vetrano, E. Koos, Role of nanoparticles in nanofluid droplet impact on solid surfaces, Langmuir 39 (1) (2023) 12–19, http://dx.doi.org/10.1021/acs.langmuir.2c02578.

[4] Y. Li, F. Wang, H. Liu, H. Wu, Nanoparticle-tuned spreading behavior of nanofluid droplets on the solid substrate, Microfluid. Nanofluid. 18 (1) (2015) 111–120, http://dx.doi.org/10.1007/s10404-014-1422-y.

[5] Y.T. Aksoy, P. Eneren, E. Koos, M.R. Vetrano, Spreading dynamics of Al_2O_3-water nanofluid droplets impacting on a smooth flat surface, in: Proceedings of the 7th World Congress on Momentum, Heat and Mass Transfer (MHMT'22), 2022, http://dx.doi.org/10.11159/enfht22.199.

[6] J. Breitenbach, I.V. Roisman, C. Tropea, From drop impact physics to spray cooling models: a critical review, Exp. Fluids 59 (3) (2018) 55, http://dx.doi.org/10.1007/s00348-018-2514-3.

[7] R. Rioboo, C. Tropea, M. Marengo, Outcomes from a drop impact on solid surfaces, At. Sprays 11 (2) (2001) 155–165, http://dx.doi.org/10.1615/AtomizSpr.v11.i2.40.

[8] C. Mundo, M. Sommerfeld, C. Tropea, Droplet-wall collisions: Experimental studies of the deformation and breakup process, Int. J. Multiph. Flow. 21 (2) (1995) 151–173, http://dx.doi.org/10.1016/0301-9322(94)00069-V.

[9] G. Liang, I. Mudawar, Review of drop impact on heated walls, Int. J. Heat Mass Transfer 106 (2017) 103–126, http://dx.doi.org/10.1016/j.ijheatmasstransfer.2016.10.031.

[10] Z. Liu, S. Li, X. Pan, H. Fang, Mechanism study on spreading dynamics of nanofluids droplet coupled with thermal evaporation, Int. J. Heat Mass Transfer 183 (2022) 122172, http://dx.doi.org/10.1016/j.ijheatmasstransfer.2021.122172.

[11] A. Gholijani, C. Schlawitschek, T. Gambaryan-Roisman, P. Stephan, Heat transfer during drop impingement onto a hot wall: The influence of wall superheat, impact velocity, and drop diameter, Int. J. Heat Mass Transfer 153 (2020) 119661, http://dx.doi.org/10.1016/j.ijheatmasstransfer.2020.119661.

[12] G. Guggilla, R. Narayanaswamy, A. Pattamatta, An experimental investigation into the spread and heat transfer dynamics of a train of two concentric impinging droplets over a heated surface, Exp. Therm Fluid Sci. 110 (2020) 109916, http://dx.doi.org/10.1016/j.expthermflusci.2019.109916.

[13] V. Nakoryakov, S. Misyura, S. Elistratov, The behavior of water droplets on the heated surface, Int. J. Heat Mass Transfer 55 (23) (2012) 6609–6617, http://dx.doi.org/10.1016/j.ijheatmasstransfer.2012.06.069.

[14] A. Gholijani, T. Gambaryan-Roisman, P. Stephan, Experimental investigation of hydrodynamics and heat transport during vertical coalescence of multiple successive drops impacting a hot wall under saturated vapor atmosphere, Exp. Therm Fluid Sci. 118 (2020) 110145, http://dx.doi.org/10.1016/j.expthermflusci.2020.110145.

[15] T. Okawa, K. Nagano, T. Hirano, Boiling heat transfer during single nanofluid drop impacts onto a hot wall, Exp. Therm Fluid Sci. 36 (2012) 78–85, http://dx.doi.org/10.1016/j.expthermflusci.2011.08.007.

[16] R.G. Jackson, M. Kahani, N. Karwa, A. Wu, R. Lamb, R. Taylor, G. Rosengarten, Effect of surface wettability on carbon nanotube water-based nanofluid droplet impingement heat transfer, J. Phys. Conf. Ser. 525 (2014) 012024, http://dx.doi.org/10.1088/1742-6596/525/1/012024.

[17] P. Pournaderi, M. Deilami, Modeling nanofluid droplet impingement on a superheated surface, Powder Technol. 381 (2021) 68–81, http://dx.doi.org/10.1016/j.powtec.2020.11.080.

[18] F. Siddiqui, C. Tso, S. Fu, H. Qiu, C.Y. Chao, Droplet evaporation and boiling for different mixing ratios of the silver-graphene hybrid nanofluid over heated surfaces, Int. J. Heat Mass Transfer 180 (2021) 121786, http://dx.doi.org/10.1016/j.ijheatmasstransfer.2021.121786.

[19] S.M.S. Murshed, C.A. Nieto de Castro, Spreading characteristics of nanofluid droplets impacting onto a solid surface, J. Nanosci. Nanotechnol. 11 (4) (2011) 3427–3433, http://dx.doi.org/10.1166/jnn.2011.3745.

[20] Y. Aksoy, P. Eneren, E. Koos, M. Vetrano, Spreading-splashing transition of nanofluid droplets on a smooth flat surface, J. Colloid Interface Sci. 606 (2022) 434–443, http://dx.doi.org/10.1016/j.jcis.2021.07.157.

[21] P. Pontes, Q.J. Liang, F.M. Matos, A.S. Moita, A.P.C. Ribeiro, A.L.N. Moreira, Heat transfer and fluid dynamics of nanofluid droplets impacting on a smooth heated surface: Detailing temporal scale effects by using time-resolved thermography, Heat Transf. Eng. 42 (19–20) (2021) 1720–1731, http://dx.doi.org/10.1080/01457632.2020.1818418.

[22] J.-Z. Jiang, S. Zhang, X.-L. Fu, L. Liu, B.-M. Sun, Microscopic experimental study of nanoparticle motion for droplet evaporation enhancement in nanofluids, Int. Commun. Heat Mass Transfer 119 (2020) 104948, http://dx.doi.org/10.1016/j.icheatmasstransfer.2020.104948.

[23] W. Chaze, O. Caballina, G. Castanet, F. Lemoine, Spatially and temporally resolved measurements of the temperature inside droplets impinging on a hot solid surface, Exp. Fluids 58 (8) (2017) 96, http://dx.doi.org/10.1007/s00348-017-2375-1.

[24] G. Castanet, T. Liénart, F. Lemoine, Dynamics and temperature of droplets impacting onto a heated wall, Int. J. Heat Mass Transfer 52 (3) (2009) 670–679, http://dx.doi.org/10.1016/j.ijheatmasstransfer.2008.07.024.

[25] A. Gholijani, T. Gambaryan-Roisman, P. Stephan, Experimental investigation of hydrodynamics and heat transport during horizontal coalescence of two drops impinging a hot wall, Exp. Therm Fluid Sci. 131 (2022) 110520, http://dx.doi.org/10.1016/j.expthermflusci.2021.110520.

[26] W. Chaze, O. Caballina, G. Castanet, J.-F. Pierson, F. Lemoine, D. Maillet, Heat flux reconstruction by inversion of experimental infrared temperature measurements - Application to the impact of a droplet in the film boiling regime, Int. J. Heat Mass Transfer 128 (2019) 469–478, http://dx.doi.org/10.1016/j.ijheatmasstransfer.2018.08.069.

[27] D.G. Cahill, S.-M. Lee, T.I. Selinder, Thermal conductivity of κ-Al_2O_3 and α-Al_2O_3 wear-resistant coatings, J. Appl. Phys. 83 (11) (1998) 5783–5786, http://dx.doi.org/10.1063/1.367500.

[28] D. Ditmars, S. Ishihara, S. Chang, G. Bernstein, E. West, Enthalpy and heat-capacity standard reference material: Synthetic sapphire (α-Al_2O_3) from 10 to 2250 K, J. Res. Natl. Inst. Stand. Technol. 87 (2) (1982) 159–163, http://dx.doi.org/10.6028/jres.087.012.

[29] J. Palacios, J. Hernández, P. Gómez, C. Zanzi, J. López, On the impact of viscous drops onto dry smooth surfaces, Exp. Fluids 52 (6) (2012) 1449–1463, http://dx.doi.org/10.1007/s00348-012-1264-x.

[30] P. Eneren, Y.T. Aksoy, Y. Zhu, E. Koos, M.R. Vetrano, Light extinction spectroscopy applied to polystyrene colloids: Sensitivity to complex refractive index uncertainties and to noise, J. Quant. Spectrosc. Radiat. Transfer 261 (2021) 107494, http://dx.doi.org/10.1016/j.jqsrt.2020.107494.

[31] A. Volk, C.J. Kähler, Density model for aqueous glycerol solutions, Exp. Fluids 59 (5) (2018) 75, http://dx.doi.org/10.1007/s00348-018-2527-y.

[32] K. Takamura, H. Fischer, N.R. Morrow, Physical properties of aqueous glycerol solutions, J. Pet. Sci. Eng. 98–99 (2012) 50–60, http://dx.doi.org/10.1016/j.petrol.2012.09.003.

[33] N.-S. Cheng, Formula for the viscosity of a glycerol-water mixture, Ind. Eng. Chem. Res. 47 (9) (2008) 3285–3288, http://dx.doi.org/10.1021/ie071349z.

[34] G. Lu, Y.-Y. Duan, X.-D. Wang, Surface tension, viscosity, and rheology of water-based nanofluids: a microscopic interpretation on the molecular level, J. Nanoparticle Res. 16 (9) (2014) 2564, http://dx.doi.org/10.1007/s11051-014-2564-2.

[35] M. Radiom, C. Yang, W.K. Chan, Dynamic contact angle of water-based titanium oxide nanofluid, Nanoscale Res. Lett. 8 (1) (2013) 282, http://dx.doi.org/10.1186/1556-276X-8-282.

[36] O.A. Alawi, N.A.C. Sidik, H.W. Xian, T.H. Kean, S. Kazi, Thermal conductivity and viscosity models of metallic oxides nanofluids, Int. J. Heat Mass Transfer 116 (2018) 1314–1325, http://dx.doi.org/10.1016/j.ijheatmasstransfer.2017.09.133.

[37] Y. Jannot, A. Degiovanni, Steady-state methods, in: Thermal Properties Measurement of Materials, John Wiley & Sons, Ltd, 2018, pp. 83–116, http://dx.doi.org/10.1002/9781119475057.ch3, Ch. 3.

[38] N.R. Sgreva, J. Noel, C. Métivier, P. Marchal, H. Chaynes, M. Isaiev, Y. Jannot, Thermo-physical characterization of Hexadecane during the solid/liquid phase change, Thermochim. Acta 710 (2022) 179180, http://dx.doi.org/10.1016/j.tca.2022.179180.

[39] J. Lv, S. Chang, C. Hu, M. Bai, P. Wang, K. Zeng, Experimental investigation of free single jet impingement using Al_2O_3-water nanofluid, Int. Commun. Heat Mass Transfer 88 (2017) 126–135, http://dx.doi.org/10.1016/j.icheatmasstransfer.2017.08.017.

[40] M. Pryazhnikov, A. Minakov, V. Rudyak, D. Guzei, Thermal conductivity measurements of nanofluids, Int. J. Heat Mass Transfer 104 (2017) 1275–1282, http://dx.doi.org/10.1016/j.ijheatmasstransfer.2016.09.080.

[41] M. Kahani, S.Z. Heris, S. Mousavi, Comparative study between metal oxide nanopowders on thermal characteristics of nanofluid flow through helical coils, Powder Technol. 246 (2013) 82–92, http://dx.doi.org/10.1016/j.powtec.2013.05.010.

[42] G. Castanet, O. Caballina, W. Chaze, R. Collignon, F. Lemoine, The Leidenfrost transition of water droplets impinging onto a superheated surface, Int. J. Heat Mass Transfer 160 (2020) 120126, http://dx.doi.org/10.1016/j.ijheatmasstransfer.2020.120126.

[43] G. Castanet, W. Chaze, O. Caballina, R. Collignon, F. Lemoine, Transient evolution of the heat transfer and the vapor film thickness at the drop impact in the regime of film boiling, Phys. Fluids 30 (12) (2018) 122109, http://dx.doi.org/10.1063/1.5059388.

[44] B.L. Scheller, D.W. Bousfield, Newtonian drop impact with a solid surface, AIChE J. 41 (6) (1995) 1357–1367, http://dx.doi.org/10.1002/aic.690410602.

[45] C. Tang, M. Qin, X. Weng, X. Zhang, P. Zhang, J. Li, Z. Huang, Dynamics of droplet impact on solid surface with different roughness, Int. J. Multiph. Flow. 96 (2017) 56–69, http://dx.doi.org/10.1016/j.ijmultiphaseflow.2017.07.002.

[46] Y.T. Aksoy, P. Eneren, E. Koos, M.R. Vetrano, Spreading of a droplet impacting on a smooth flat surface: How liquid viscosity influences the maximum spreading time and spreading ratio, Phys. Fluids 34 (4) (2022) 042106, http://dx.doi.org/10.1063/5.0086050.

[47] M. Batmunkh, M.R. Tanshen, M.J. Nine, M. Myekhlai, H. Choi, H. Chung, H. Jeong, Thermal conductivity of TiO2 nanoparticles based aqueous nanofluids with an addition of a modified silver particle, Ind. Eng. Chem. Res. 53 (20) (2014) 8445–8451, http://dx.doi.org/10.1021/ie403712f.

[48] V. Wanatasanapan, M. Abdullah, P. Gunnasegaran, Effect of TiO2-Al2O3 nanoparticle mixing ratio on the thermal conductivity, rheological properties, and dynamic viscosity of water-based hybrid nanofluid, J. Mater. Res. Technol. 9 (6) (2020) 13781–13792, http://dx.doi.org/10.1016/j.jmrt.2020.09.127.

[49] Y.T. Aksoy, H. Cornelissen, P. Eneren, M.R. Vetrano, Spray cooling investigation of TiO_2-water nanofluids on a hot surface, Energies 16 (7) (2023) http://dx.doi.org/10.3390/en16072938.

[50] R. Hedge, S. Rao, R. Reddy, Flow visualization and study of CHF enhancement in pool boiling with Al_2O_3 - Water nano-fluids, Therm. Sci. 16 (2) (2012) 445–453, http://dx.doi.org/10.2298/TSCI100511095H.

[51] P. Eneren, Y.T. Aksoy, M.R. Vetrano, Experiments on single-phase nanofluid heat transfer mechanisms in microchannel heat sinks: A review, Energies 15 (7) (2022) http://dx.doi.org/10.3390/en15072525.

[52] W. Ajeeb, S.M.S. Murshed, Pool boiling heat transfer characteristics of new and recycled alumina nanofluids, Nanomaterials 13 (6) (2023) http://dx.doi.org/10.3390/nano13061040.